Study of the Crystal Structure of SnS Thin Films by Atomic Layer Deposition

Study of the crystal structure of SnS thin films by atomic layer deposition

Xizhu Zhao,[1,†] Luke M. Davis,[1,§] Xiabing Lou,[1,‡] Sang Bok Kim,[1,+] Sona Ulicna,[2] Ashwin Jayaraman,[1,#] Chuanxi Yang,[1,∂] Laura T. Schelhas,[2] and Roy Gordon[1,*]

1. *Harvard University, Cambridge, MA 02138, USA*
2. *SLAC National Accelerator Laboratory, Menlo Park, CA 94025, USA*

[*] *Corresponding author's email address: gordon@chemistry.harvard.edu*

Abstract. Tin monosulfide, SnS, absorbs visible light and holds promise for thin-film photovoltaics. However, the optoelectronic properties of this material vary among the different structural phases, and control over the phase of vapor deposited SnS thin films is not well understood. In order to study the phases and crystallographic orientations of SnS films, films with thicknesses of 90 nm to 750 nm were prepared by atomic layer deposition (ALD) at temperatures between 80 and 200 °C on amorphous silicon dioxide (a-SiO_2) and single-crystal sodium chloride (NaCl). We show that the crystal structures and orientations of the ALD-SnS thin films vary with deposition temperature, film thickness, and substrate. We confirm the presence of metastable cubic π-SnS in co-existence with the thermodynamically stable orthorhombic α-SnS, and find that the π phase is more prevalent at lower deposition temperatures. The films grown on a-SiO_2 are textured and the degree of texturing increases with lower temperature or higher thickness, and the deposited phase is also thickness dependent. Upon annealing, which is known to promote SnS grain growth, all films revert to orthorhombic α-SnS. The films grown on the NaCl(100) substrate exhibit a much higher degree of texturing and show different preferred orientations dependent on the phase: π-(400) and α-(111) or (040). In addition, we demonstrate a proof-of-concept device made from the highly oriented SnS grown on NaCl.

Tin monosulfide (SnS) has demonstrated strong potential as a photovoltaic light absorber due to its high absorption coefficient and simple binary system with only non-toxic and earth-abundant elements. [1-7] These features make SnS a promising PV absorber candidate when compared with the commercially available CdTe and CIGS thin film solar

cells and the emerging halide perovskites. The optoelectronic properties of SnS thin films and of the solar cells made from it vary across a wide range depending on the cell structure and the film deposition methods, with a record efficiency of 4.4% (certified) [3] and 5.2% (uncertified) [8].

SnS is a p-type IV-VI semiconductor. Its thermodynamically stable orthorhombic crystal structure (α) consists of double layers where tin and sulfur atoms are covalently bonded in-plane and loosely connected with van der Waals forces in the out-of-plane direction. This layered structure gives rise to strongly anisotropic properties, where the in-plane electrical conductivity and Hall mobility are five to six times higher than those along the out-of-plane axis. [9] On this basis, it is hypothesized that control of the SnS orientation may be important in solar cell applications. When the in-plane axis is oriented perpendicular to the substrate, carrier transport through the absorber should be faster and carriers should be collected more efficiently by the electron and hole transport layers.

In addition, the orthorhombic crystal structure leads to an indirect bandgap of 1.1 eV, which is 0.2 – 0.3 eV below its effective absorption onset (i.e., direct gap), leading to a thermalization loss in the open circuit voltage. The cubic phase of SnS has long been known to the scientific community; it is isotropic and has a calculated direct bandgap of 1.3 – 1.7 eV. [10, 11] Earlier researchers disagreed about whether it is of rock-salt (rs) or zinc-blende structure (zb). [5, 12-19] A new cubic phase (π) of SnS comprising 64 atoms in a unit cell and a lattice constant of 11.7 Å, [20] was proposed to resolve the previous rock-salt/zinc-blende confusion and has since gained increasing acceptance. [10, 11, 21-26] A common approach to targeting desired phases is the use of epitaxial growth. It is well known that polymorphism of crystalline films could be induced by stress or epitaxial growth on a lattice-matched substrate. However, among the epitaxial SnS growth literatures, only the α-phase has been reported on substrates including NaCl, MgO, GaAs, and Si using vacuum deposition methods at relatively high temperatures. [14, 15, 27-29]

When utilizing SnS as the light-absorbing layer of a photovoltaic device, it is important to maximize the rate of charge transport from the point of electron-hole generation to the charge collectors to achieve more efficient charge collection. To this end, a preference emerges for either the cubic phase with its isotropic structure and direct bandgap, or the orthorhombic phase in the orientation having its SnS layers aligned perpendicular to the substrate. Our previous work touched upon the dependence of SnS orientation on substrate and crystal structure on growth temperature. [30, 31] In this study, we provide additional examination of the orientation dependence of orthorhombic SnS in relation to

temperature and film thickness, and demonstrate a highly textured growth of cubic SnS on a single-crystal NaCl substrate using atomic layer deposition at 120 °C. We also demonstrate a proof-of-concept solar cell using the cubic SnS grown on the NaCl substrate.

SnS thin films were deposited by ALD using alternating doses of bis(*N*,*N*′-diisopropylformamidinato)tin(II) and 4% H_2S in N_2 in a custom-built hot wall reactor operated in closed-valve mode. The detailed precursor properties, reactor setup, and film composition properties can be found in our previous work. [32] SnS films of thicknesses between 90 and 750 nm were deposited under temperatures ranging from 80 to 200 °C with thermally oxidized silicon (a-SiO_2) and single-crystal NaCl(100) as substrates. Field emission scanning electron microscopy (FESEM, Supra55VP) was used to examine film morphology and estimate thickness. As described previously, film growth rate is higher at lower temperatures. [32]

High-resolution X-ray diffraction (HRXRD, Bruker D8, Cu-Kα λ = 1.542 Å) θ-2θ scans were performed on all of the films, and the peak positions were compared with the reference diffraction peak positions of α-SnS, rs-SnS and π-SnS (see SI figure S1 and S2 for more details) to determine the crystal phase and orientation. Synchrotron-based 2DXRD (λ = 0.9744 Å) was performed on selected films at beamline 11-3 at the Stanford Synchrotron Radiation Lightsource (SSRL). Note that the XRD spectra are plotted in both the conventional Cu-Kα 2θ and the λ-independent q axis for easier comparison between the data collected at two different X-ray energies, where 2θ is use as the primary axis for the 1D spectra taken with Bruker D8, and q is used as the primary axis for the 2D spectra taken in SSRL. The conversion between the two axes can be found in SI Equation S1 and SI Table S1.

As deposition temperature increased from 80 °C to 200 °C, we observed that the dominant phase of SnS changed from the cubic π phase to the orthorhombic α phase, as shown in figure 1a. This finding agrees with other studies about the dependence of SnS crystal structure on growth temperature. [19, 22-24] Furthermore, these θ-2θ scans also provide a direct assessment of the out-of-plane film orientation. At lower temperatures of 80 °C – 120 °C only the cubic phase peaks can be seen. Within this temperature range, the π-(222) peak at 2θ = 26.6° is the only dominant peak for the 80 °C film, while the π-(400) peak at 30.8° becomes more apparent in the 120 °C film, indicating reduced texturing in the π-SnS as temperature increases. As temperature is further increased from 120 °C to 200 °C, the π peaks gradually disappear while the α-(120) and α-(040) peaks increase in intensity.

To further characterize the phases and examine the film orientation (texturing) as a function of temperature, SnS thin films, 120 nm thick, were deposited at 80 °C and 120 °C and examined with the Synchrotron 2DXRD at SLAC. Analysis by eye of the 2D patterns shows little obvious difference between the two films. To further parse out the differences in these films the 2D XRD patterns were integrated to 1D powder patterns (figure 1c). From the powder patterns we can see that the pattern from the film deposited at 80 °C corresponds more closely to the reference powder pattern for the π phase in terms of both peak positions and relative intensities. In contrast, the pattern from the film deposited at 120 °C has a less prominent π-(222) peak but has shoulders corresponding to the α-(120) and α-(021) peaks. Also, the peak intensity around 31.8° was stronger than would be expected from the reference π-SnS pattern, [21] likely indicating existence of the α-(111) or α-(040) peak together with the π-(410) peak at 31.8°. Both the HRXRD θ-2θ scans and the 2DXRD spectra demonstrate that a phase transition from π to α occurs with an increase in growth temperature.

Film thickness is another factor that yields a phase transition and orientation change in the SnS thin films. In previous work we reported that the preferred orientation of thin films changed from α-(040) to α-(111) as film thickness increased. [7] In this work we took a close look at films deposited at 80 °C, where the cubic phase was present. As shown in figure 2, only the π-(222) peak was evident in the 140 nm thick film deposited at 80 °C; the co-existence of both π and α phases was evident in the 320 nm thick film; and as the film thickness further increased, the π-peak intensity kept decreasing and the α-(002) became the only major peak. This result is consistent with a transformation from π-SnS to α-SnS as film thickness increases.

The above results show that π-SnS is the dominant phase only in very thin films, not sufficiently thick for a good photovoltaic absorber, and raise the concern that the π-SnS might not persist under the high-temperature annealing conditions previously used for absorber grain growth necessary to enhance solar cell power conversion efficiency. [7] Indeed, as we recently reported, [32] the standard anneal [3, 4] of 400 °C under 10 Torr of 2.5% H_2S in nitrogen promotes grain growth, but also converts the π-SnS to α-SnS. Therefore, we explored a lattice-matched substrate to induce epitaxial growth of π-SnS as an alternative method to achieve high quality π-SnS films for application in a thin film SnS solar cell. NaCl(100) is the most used substrate in the limited literature found on epitaxial growth of α-SnS. NaCl has a lattice constant of 5.64 Å (PDF 05-0628), causing a mismatch of less than 3% with the previously reported rock-salt SnS (PDF 01-077-3356, a = 5.80Å) and less than 4% with the new π-SnS [10] (a = 11.7Å). After successful

deposition of a thin π-SnS on the amorphous thermal oxide substrate at low temperature, a thicker SnS film (600 nm) was deposited on the NaCl(100) substrate, with the hypothesis that the lattice matched NaCl substrate would deter the phase transition as thickness increases and induce epitaxial growth of π-SnS.

Single crystals of NaCl were obtained in 1 cm^3 cubes from Ted Pella Inc. and cleaved with a razorblade into 3 mm slabs to reveal a clean (100) surface. It was then immediately placed into the reactor next to a piece of O_2-plasma treated thermal oxide substrate. SEM images of 12000 cycles of SnS deposited on NaCl(100) and thermal oxide substrates (figure 3) showed clear differences in morphology—the film grown on SiO_2 substrate had columnar grains with smaller grain size especially in the region near the substrate, while the film grown on NaCl had larger grain size. The film on NaCl was also slightly thinner, possibly due to different durations of the initial nucleation delay. [32]

As shown in the synchrotron 2DXRD spectra (figure 4a), the film grown on NaCl shows almost single-crystalline features of spots spaced evenly on each of the rings corresponding to different 2θ values. Looking at the 2D images and the integrated patterns (figure 4b), we could conclude that on NaCl substrate, the film exhibits highly textured growth in the <100> direction of the π phase, as manifested in the spots along the corresponding ring. However, on thermal oxide substrate, the film is only moderately textured with the π-{111} plane dominating the crystal planes parallel to the substrate. One remaining issue is that the NaCl(200) substrate peak overlaps with several major SnS peaks of both the α and π phases and obscures what is truly happening. Thus, a high resolution XRD θ-2θ scan was taken again after dissolving the substrate in water and is presented in figure 5. Two peaks in the region of 31.5° – 32° appeared, which align well with the α-(111) (31.5°) and α-(040) (32.0°) peaks, and the π-(410) peak at 31.8° could have also been present. We thus conclude that the film grown on NaCl comprises mixed phases of α and π, and the grains are highly textured in the π-(410) or α-(111) and (040) directions out-of-plane. While we cannot rule out the possibility that dissolving the NaCl substrate *induces* a partial phase transformation, the above conclusion is a conservative interpretation of the data – at a minimum, some portion of the film is grown as highly textured π-SnS.

After annealing in an H_2S environment, the films grown on both NaCl and thermal-oxide substrates are converted to the α phase as shown in SI figure S6. The film on NaCl substrate also lost some of its texturing and suffers delamination, rendering this annealed film unfit for solar cell application. Nevertheless, the near-epitaxial π-SnS grown on NaCl(100) substrates could be a promising light absorber. A solar cell was fabricated using the SnS grown

on NaCl and its J-V results are presented in figure 6. The SnS absorber layer (600 nm) and the Zn(O,S):N buffer layer were deposited by ALD at 120 °C. Then 300 nm of ITO were sputtered on the film to make the window layer, and 500 nm of Ag were evaporated as the front contact. Details of the buffer, window, and front contact layers can be found in [3, 4]. A fabrication schematic is shown in SI figure S7. The current−voltage (J−V) characteristics were measured using Agilent 4156C and Keithley 2400 semiconductor characterization systems under 100 mW/cm^2 AM 1.5G illumination. The cell demonstrates an open circuit voltage of 670 mV, remarkable for being nearly a factor of two higher than the V_{OC} observed for annealed α-SnS in the current record devices. [3, 8] The short circuit current density is on the order of 100 nA/cm^2, which is 4-5 orders of magnitude lower than the J_{SC} of a normal functioning solar cell made from SnS reported in literature [6]. The low current density could be due to the high series resistance caused by a low carrier density of the π-SnS and/or the low quality of the front and back contact, which also causes large variations between measurements. We should note that the seemingly high V_{OC} could be due to a capacitance effect, and a SunsV_{OC} measurement could be conducted to further examine this effect. Nonetheless, we demonstrated feasibility of fabricating a solar cell device with π-SnS by growing the absorber layer atop the nonconductive yet water soluble NaCl substrate.

In summary, it is demonstrated that the phase and orientation of a SnS film are determined by the combined effect of temperature, film thickness, and substrate type. The film grown on thermal oxide is textured but the degree of texturing decreases as temperature increases, and the preferred phase-orientation is dependent on both thickness and temperature. Near-epitaxial growth of π-SnS can be obtained by growing on a lattice matched NaCl(100) substrate, although the films also contains the α-phase after being released from the NaCl substrate. We also demonstrated a proof-of-concept solar cell fabricated from the π-SnS grown on NaCl with potential improvement of open circuit voltage compared with record devices. Challenges remain in reducing the series resistance of the cell and improving the contact quality as well as the reliability of the fabrication process. Studies are ongoing to further optimize the deposition conditions to obtain phase-pure epitaxial π-SnS or well-orientated α-SnS films to improve carrier transport through the absorber layer.

Supporting Information

Crystallographic structures and lattice parameters of SnS, reference XRD patterns of SnS and NaCl (PDF), complementary XRD patterns of SnS film grown on thermal oxide and NaCl, schematics of solar cell fabrication procedure, and complementary J-V measurement.

Data Availability

The data that supports the findings of this study are available within the article and its supplementary material.

Acknowledgements

Funding for this study was provided in part by the Center for Next Generation of Materials Design, an Energy Frontier Research Center funded by the U.S. DOE, Office of Science, under contract no. UGA-0-41029-16/ER392000. Part of the characterization was performed at Harvard University's Center for Nanoscale Systems, a member of the National Nanotechnology Coordinated Infrastructure Network, which is supported by the NSF under ECCS-1541959. Use of the Stanford Synchrotron Radiation Lightsource, SLAC National Accelerator Laboratory, was supported by the U.S. Department of Energy, Office of Basic Energy Sciences under Contract No. DE-AC02-76SF00515.

Author Information

Corresponding Author

* gordon@chemistry.harvard.edu.

Present Addresses

† LAM Research, 4650 Cushing Pkwy, Fremont, CA 94538, USA.
§ Department of Chemistry, Tufts University, 62 Talbot Avenue, Medford, MA 02155, USA.
‡ Cambridge Electronics, Inc., 501 Massachusetts Avenue, Cambridge, MA 02139, USA.
$^{+}$ Center for Educational Research, Seoul National University, 1 Gwanak-ro, Gwanak-gu, Seoul 08826, Korea
Argonne National Laboratory, 9700 S Cass Avenue, Lemont, IL 60439, USA.
∂ Applied Materials, Inc., 3050 Bowers Avenue, Santa Clara, CA 95054, USA.

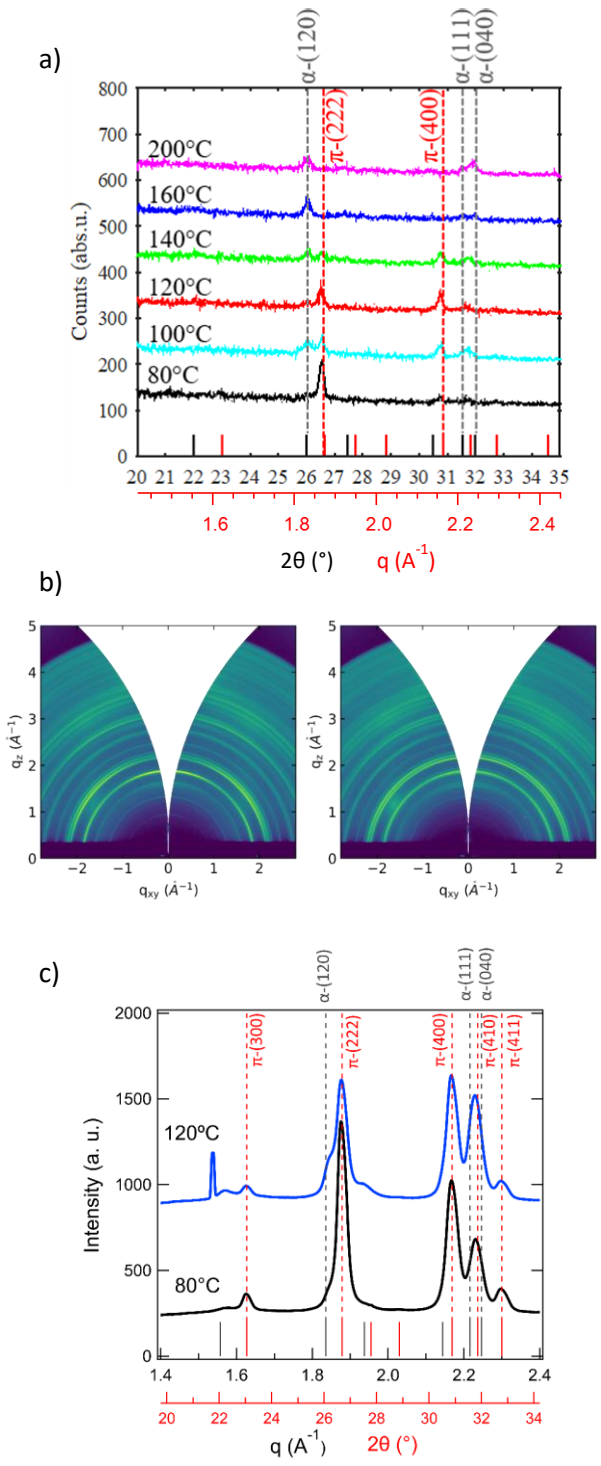

Figure 1. XRD patterns of 2000 ALD cycles (150 nm – 90 nm) of SnS deposited at 80 °C – 200 °C on thermal oxide substrates. (a) θ-2θ scans in the range of 2θ = 20° – 35°. (b) Synchrotron 2DXRD images of the two films deposited at 80 and 120 °C. (c) Integrated patterns from the 2DXRD images in the range of 2θ = 20° – 35°. Wider patterns in the range of 2θ = 20° – 60° of the films in (a) and (c) are provided in SI figure S3. The solid colored lines at the bottom of (a) and (c) indicate power diffraction peak positions of the α (black) and π (red) phases; reference power diffraction patterns can be found in SI figure S2.

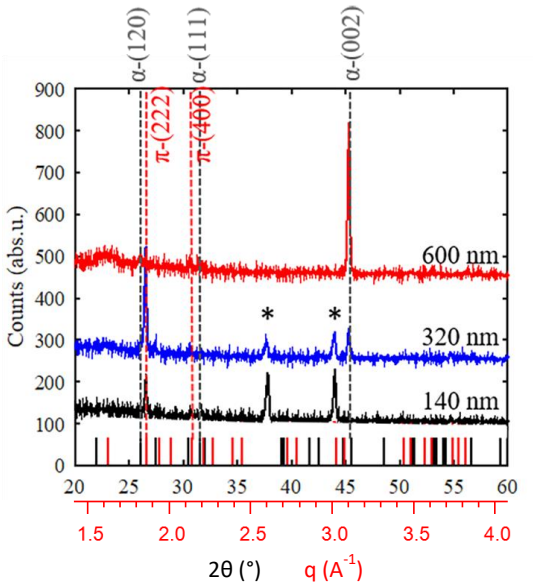

Figure 2. XRD θ-2θ scans of SnS of different thicknesses deposited at 80 °C on thermal oxide substrate. The asterisks (*) mark the peaks from the substrate holder of the XRD equipment. A zoomed-in image in the range of 2θ = 20° – 35° can be found in SI figure S4 to show the peaks in that range more clearly.

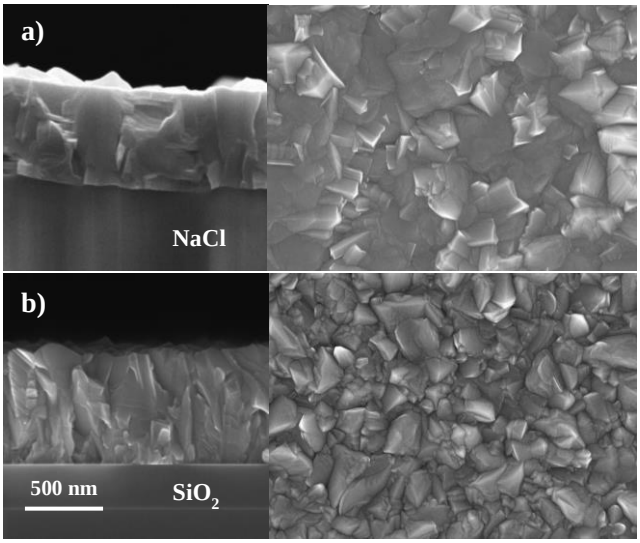

Figure 3. Cross-sectional and plan-view SEM of 12000 cycles of SnS deposited on (a) NaCl(100) substrate and (b) thermal oxide substrate at 120 ℃.

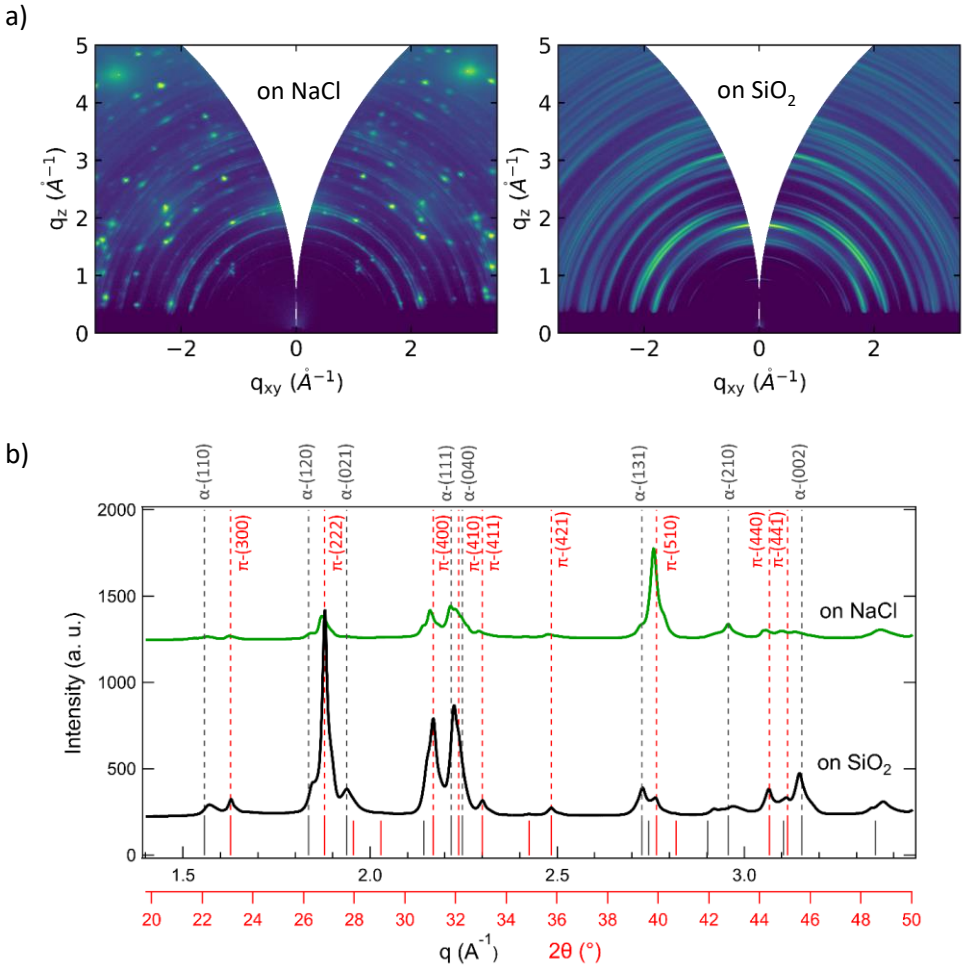

Figure 4. (a) Synchrotron 2DXRD patterns of 12000 cycles of SnS films deposited at 120 °C on thermal-oxide and NaCl(100) substrates. (b) Integrated θ-2θ patterns from the 2DXRD images in the range of 2θ = 20° – 50°. 2DXRD and integrated θ-2θ patterns of these two films after annealing can be found in SI figure S6. 2DXRD patterns of bare NaCl(100) and thermal-oxide substrates can be found in SI figure S5.

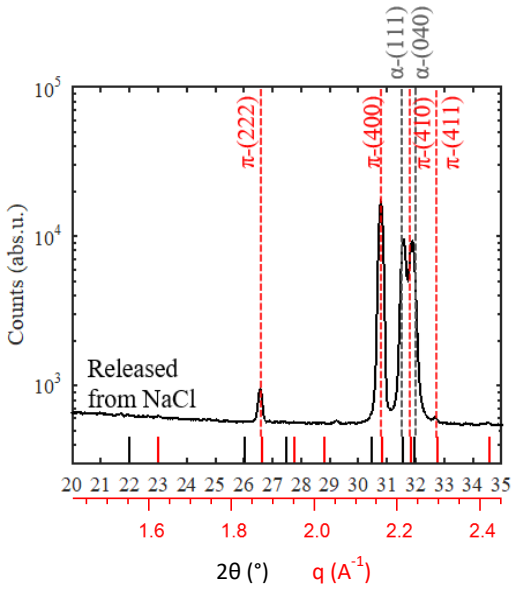

Figure 5. θ-2θ scan of the film deposited at 120 °C on NaCl(100) after releasing from the substrate.

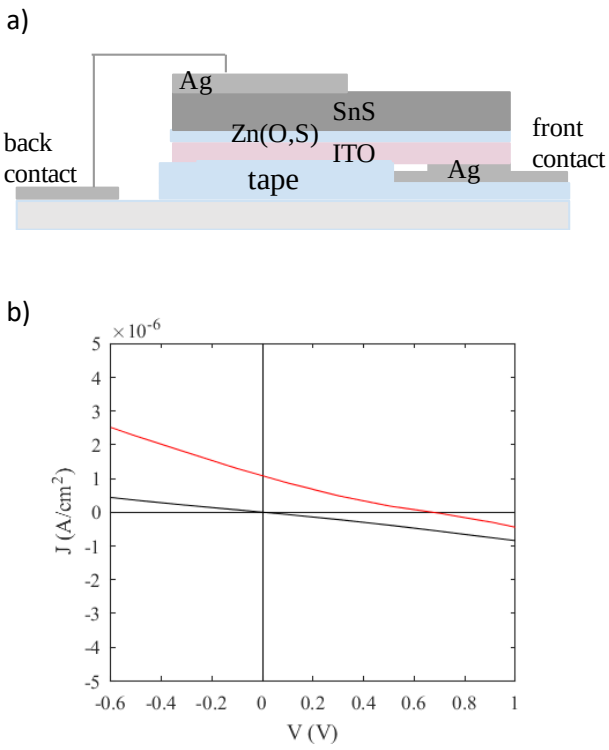

Figure 6. Solar cell using π-SnS grown on NaCl (100) substrate. (a) Schematics of the final cell structure. (b) J-V measurement under dark condition (black) and under 1 sun (AM 1.5) illumination (red). A J-V curve with -10 V to 10 V voltage scan that shows clearer diode behavior can be found in SI figure S8.

References

1. H. Noguchi, A. Setiyadi, H. Tanamura, T. Nagatomo, and O. Omoto, Solar Energy Materials and Solar Cells **35**, 325 (1994).

2. K.T.R. Reddy, N.K. Reddy, and R.W. Miles, Solar Energy Materials and Solar Cells **90**(18–19), 3041 (2006).

3. P. Sinsermsuksakul, L. Sun, S. W. Lee, H. H. Park, S, B. Kim, C. Yang, and R. G. Gordon, Advanced Energy Materials **4**(15), 1400496 (2014).

4. R. Jaramillo, V. Steinmann, C. Yang, K. Hartman, R. Chakraborty, J. R. Poindexter, M. L. Castillo, R. Gordon, and T. Buonassisi, J Vis Exp **99**, e52705 (2015).

5. R. E. Banai, M.W. Horn, and J.R.S. Brownson, Solar Energy Materials and Solar Cells **150**, 112 (2016).

6. S. Di Mare, D. Menossi, A. Salavei, E. Artegiani, F. Piccinelli, A. Kumar, G. Mariotto, and A. Romeo, Coatings **7**(12), 34 (2017).

7. P. Sinsermsuksakul, J. Y. Heo, W.Noh, A. S. Hock, and R. G. Gordon, Advanced Energy Materials **1**(6), 1116 (2011).

8. X. Zhao, Ph.D. Thesis, Harvard University (2018).

9. W. Albers, C. Haas, H. J. Vink, and J. D. Wasscher, Journal of Applied Physics **32**(10), 2220 (1961).

10. J. M. Skelton, L. A. Burton, F. Oba, and A. Walsh, J Phys Chem C Nanomater Interfaces, **121**(12), 6446 (2017).

11. R. E. Abutbul, E. Segev, L. Zeiri, V. Ezersky, G. Makovab and Y. Golan, RSC Advances **6**(7), 5848 (2016).

12. L. A. Burton, and A. Walsh, The Journal of Physical Chemistry C **116**(45), 24262 (2012).

13. S. B. Badachhape and A. Goswami, Journal of the Physical Society of Japan **17 Suppl. B-II** (1962).

14. A. N. Mariano and K. L. Chopra, Applied Physics Letters **10**(10), 282 (1967).

15. B. F. Bilenkii, A.G. Mikolaichuk, and D.M. Freik, phys. stat. sol. **28**(K5), (1968).

16. M. Devika, N. K. Reddy, K. Ramesh, H. R. Sumana, K. R. Gunasekhar, E. S. R. Gopal and K. T. R. Reddy, Semiconductor Science and Technology **21**(10), 1495 (2006).

17. D. Avellaneda, M. T. S. Nair, and P. K. Nair, Journal of The Electrochemical Society **155**(7), D517 (2008).

18. C. Gao, H. Shen, L. Sun, H. Huang, L. Lu and H. Cai, Materials Letters **64**(20), 2177 (2010).

19. E. C. Greyson, J. E. Barton and T. W. Odom, Small **2**(3), 368 (2006).

20. A. Rabkin, S. Samuha, R. E. Abutbul, V. Ezersky, L. Meshi and Y. Golan, Nano Lett **15**(3), 2174 (2015).

21. R. E. Abutbul, A. R. Garcia-Angelmo, Z. Burshtein, M. T. S. Nair, P. K. Nair and Y. Golan, CrystEngComm **18**(27), 5188 (2016).

22. Nair, P.K., A.R. Garcia-Angelmo, and M.T.S. Nair, physica status solidi (a) **213**(1), 170 (2016).

23. O. V. Bilousov, Y. Ren, T. Törndahl, O. Donzel-Gargand, T. Ericson, C. Platzer-Björkman, M. Edoff and C. Hägglund, Chemistry of Materials **29**(7), 2969 (2017).

24. I. H. Baek, J. J. Pyeon, Y. G. Song, T. M. Chung, H. R. Kim, S. H. Baek, J. S. Kim, C. Y. Kang, J. W. Choi, C. S. Hwang, J. H. Han and S. K. Kim, Chemistry of Materials **29**(19), 8100 (2017).

25. K. O. Hara, S. Suzuki and N. Usami, Thin Solid Films **639** 7 (2017).

26. J. M. Skelton, L. A. Burton, F. Oba and A. Walsh, APL Materials **5**(3), 036101 (2017).

27. A. Wangperawong, S. M. Herron, R. R. Runser, C. Hägglund, J. T. Tanskanen, H. B. R. Lee, B. M. Clemens and S. F. Bent, Applied Physics Letters **103**(5). 052105 (2013).

28. F. Y. Ran, Z. Xiao, H. Hiramatsu, H. Hosono and T. Kamiya, Applied Physics Letters **104**(7), 072106 (2014).

29. W. Wang, K. K. Leung, W. K. Fong, S. F. Wang, Y. Y. Hui, S. P. Lau, Z. Chen, L. J. Shi, C. B. Cao and C. Surya, Journal of Applied Physics **111**(9), 093520 (2012).

30. C. Yang, L. Sun, R. E. Brandt, S. B. Kim, X. Zhao, J. Feng, T. Buonassisi and R. G. Gordon, Journal of Applied Physics **122(4)**, 045303 (2017).

31. H. H. Park, R. Heasley, L. Sun, V. Steinmann, R. Jaramillo, K. Hartman, R. Chakraborty, P. Sinsermsuksakul, D. Chua, T. Buonassisi and R. G. Gordon, Prog.Photovolt:Res.Appl. **23**, 901 (2015).

32. S. B. Kim, X. Zhao, L. M. Davis, A. Jayaraman, C. Yang and R. G. Gordon, Applied Materials and Interfaces **11**(49), 45892 (2019).